

Numerical simulation of atmospheric Lamb waves generated by the 2022 Hunga-Tonga volcanic eruption

Angel Amores¹, Sebastian Monserrat², Marta Marcos^{1,2}, Daniel Argüeso²,
Joan Villalonga³, Gabriel Jordà³ and Damià Gomis^{1,2}.

¹Instituto Mediterráneo de Estudios Avanzados (UIB-CSIC), Esporles, Spain.

²Departament de Física (UIB), Palma, Spain.

³Centre Oceanogràfic de Balears, Instituto Español de Oceanografía (IEO-CSIC), Palma, Spain

Key Points:

- The underwater Hunga-Tonga volcano exploded generating Lamb waves that traveled around the Earth several times.
- We simulate these waves using a hydrostatic shallow water equation oceanic model.
- The results closely follow the observations of atmospheric pressure perturbations.

Corresponding author: Angel Amores, angel.amores@uib.es

This article has been accepted for publication and undergone full peer review but has not been through the copyediting, typesetting, pagination and proofreading process, which may lead to differences between this version and the [Version of Record](#). Please cite this article as [doi: 10.1029/2022GL098240](https://doi.org/10.1029/2022GL098240).

This article is protected by copyright. All rights reserved.

Abstract

On January 15th, 2022, around 4:30 UTC the eruption of the Hunga-Tonga volcano, in the South Pacific Ocean, generated a violent underwater explosion. In addition to tsunami waves that affected the Pacific coasts, the eruption created atmospheric pressure disturbances that spread out in the form of Lamb waves. The associated atmospheric pressure oscillations were detected in high-frequency in-situ observations all over the globe. Here we take advantage of the similarities in the propagation and characteristics between atmospheric Lamb waves and long ocean waves and we use a 2DH ocean numerical model to simulate the phenomenon. We compare the outputs of the numerical simulation with in-situ atmospheric pressure records and with remote satellite observations. The signal in the model matches the observed atmospheric pressure perturbations and reveals an excellent agreement in the wave arrival time between model and observations at hundreds of locations at different distances from the origin.

Plain Language Summary

The underwater explosion of the Hunga-Tonga volcano in the South Pacific Ocean generated atmospheric pressure disturbances, known as Lamb waves, that propagated and surrounded the globe several times. In this study, we exploit the similarities between atmospheric Lamb waves and long waves in the ocean (e.g., tsunamis) to simulate their propagation using an ocean numerical model. The comparison of our results with remote satellite data and in-situ atmospheric pressure records reveals that our model correctly reproduces the propagation of the atmospheric disturbances generated by the volcano explosion.

1 Introduction

On January 14th, 2022 the underwater Hunga-Tonga volcano, located in the South Pacific Ocean, erupted in a one-in-a-thousand year event (Klein, 2022). The volcano, located between the uninhabited islands of Hunga Tonga and Hunga Ha'apai of the Kingdom of Tonga, is part of the Tonga–Kermadec Islands volcanic arc and has been active since its first historical eruption in 1912 (Global Volcanism Program, 2022). The volcano had emerged after an eruption that started in December 2014. This recent eruption resulted in material being deposited and merged with the Hunga Ha'apai island, creating an area of around 2 km of diameter and maximum height of 120 m above sea level (Cronin et al., 2017). According to the Global Volcanism Program (2022), the strongest eruption began on January 15th around 17:30 local time (4:30 UTC) with a plume reaching 30 km in the atmosphere and 600 km in diameter, making it visible by multiple satellite observations. Observations of Sentinel-2 satellites revealed massive changes in the surface area and the disappearance of the formerly deposited volcanic material. The explosive eruption, whose power has been estimated to be equivalent to somewhere between 4 to 18 megatons of TNT (<https://earthobservatory.nasa.gov/images/149367/dramatic-changes-at-hunga-tonga-hunga-haapai>), generated tsunami waves (warnings were issued across several countries in the Pacific coasts) and also atmospheric shock waves that propagated across the globe and were detected by the NASA Aqua satellite as concentric wave patterns (Adam, 2022).

Such amount of energy liberated into the atmosphere by the violent eruption is expected to generate various types of atmospheric waves with different spectral energy content, including inertia gravity waves, infrasound waves and Rossby waves, making the atmospheric wave pattern close to the source very intricate. Among these atmospheric perturbations, the type of wave which is expected to optimally transfer energy over long distances, and therefore the one expected to dominate far away from the source, is the Lamb wave mode, which was first introduced by Horace Lamb (Lamb, 1881). This has been observed in earlier similar events, as for example the well-known Krakatoa volcanic

eruption in 1883 (Symons, G. J. (ed.), 1888; Press & Harkrider, 1966). The explosion-induced atmospheric waves after Krakatoa eruption circled the Earth three times (Murty, 1977) and generated tsunami waves which, at many locations, were coupled with the tsunami generated by the ocean surface perturbation provoked after the eruption (see Monserrat et al. (2006) and other references mentioned there).

Lamb waves are non-dispersive atmospheric waves, whose energy is optimally transmitted far away from the source with minor losses. They arise as solutions of the momentum equations with zero vertical velocity, meaning that Lamb waves have purely horizontal motion, occupying the full depth of the troposphere and with a maximum pressure signal at the surface. These waves are only slightly affected by the Earth's rotation and travel at the speed of sound in the media (Gossard & Hooke, 1975). Assuming an isothermal troposphere, the phase velocity of the Lamb waves, C_T , is only affected by the air temperature and is defined as:

$$C_T = \sqrt{\frac{\gamma \cdot R \cdot T}{M}}, \quad (1)$$

where $\gamma = 1.4$ is the ratio of specific heat of air corresponding to the range of atmospheric temperatures, $R = 8314.36 \text{ J} \cdot \text{kmol}^{-1} \cdot \text{K}^{-1}$ is the universal gas constant, $M = 28.966 \text{ kg} \cdot \text{kmol}^{-1}$ is the molecular mass for dry air and T is the absolute temperature.

Due to their particular characteristics, the propagation of Lamb waves through the atmosphere with spatially varying temperature is analog to the behavior of oceanic long waves propagating over an ocean with variable depth. Long waves in the ocean are also non-dispersive barotropic waves traveling with a phase velocity, C_H , given by

$$C_H = \sqrt{g \cdot H}, \quad (2)$$

where $g = 9.81 \text{ m} \cdot \text{s}^{-2}$ is the gravity acceleration and H is the ocean depth.

Long waves in the ocean have been successfully simulated using 2DH shallow water equation models, as for example, the propagation of tsunami waves and their arrival times at remote coastal locations (e.g. Titov et al. (2005)).

Given these similarities between atmospheric Lamb waves and oceanic shallow water waves, we propose to simulate the atmospheric Lamb wave generated after the Hunga-Tonga volcano explosion using a vertically-integrated hydrodynamic ocean model. To do so, a simple relationship between the vertically integrated atmospheric temperature and the equivalent ocean depth is obtained from eq. (1) and (2)

$$H = \frac{\gamma \cdot R \cdot T}{M \cdot g}, \quad (3)$$

This study is organized as follows: in Section 2 the data and the model used for the simulations as well as the way it was initialized are described. Results of the simulations are compared with remote and in-situ observations in Section 3 and a summary and conclusions are presented in Section 4.

2 Data and Methods

The numerical ocean hydrodynamic model SCHISM (Semi-implicit Cross-scale Hydroscience Integrated System Model, V5.9.0; Y. J. Zhang et al. (2016)) was used to simulate the atmospheric Lamb waves generated by the volcano explosion. We have used its dynamic core, which is a derivative product built from the original SELFE (v3.1dc; Y. Zhang and Baptista (2008)), in 2DH barotropic mode. It solves the vertically-integrated hydrostatic Navier-Stokes equations with shallow water approximation. The model domain covers the entire globe with an unstructured triangular computational grid of 0.25°

104 resolution with 1036800 nodes and 2070720 elements. The simulation starts on January
105 15th 2022 at 04:30 UTC coinciding with the volcano explosion and has a duration of 5
106 days. The computational time step was set to 1 min and the variables were saved ev-
107 ery 5 min at each computational grid point. We decided to use an oceanic model because
108 the atmospheric models suited for this kind of simulations include filters that remove fast
109 waves, such as sound waves, to avoid numerical instabilities and to allow larger time-steps.
110 It would be necessarily to adapt an atmospheric model by modifying its dynamical core
111 to represent Lamb waves. On the other hand, the numerical model we are using here is
112 specifically designed to resolve high-speed long waves, such as tsunami waves. Because
113 Lamb waves and tsunami waves behave similarly in many aspects, it was immediate to
114 adapt the model configuration to solve Lamb waves generated by the volcano explosion.
115 Moreover, the numerical model used here is vertically integrated, which makes it com-
116 putationally less demanding than using a full 3-D atmospheric global model.

117 To define the equivalent water depth in the model (see equation 3), we used the
118 atmospheric temperature fields obtained from ERA5 reanalysis . ERA5 is a comprehen-
119 sive reanalysis that spans from 1979 to near-real time and integrates historical observa-
120 tions into global estimates using advanced modeling and data assimilation systems. ERA5
121 data is provided at 1-hour temporal resolution and 0.25° spatial resolution. A time-varying
122 temperature field over the domain was defined to represent the vertically-averaged at-
123 mospheric temperature. For the results shown, the simplest approach was taken. The
124 temperature field has been computed as the average between the temperature at 2 m (ob-
125 tained from ERA5 data on single levels; Hersbach et al. (2018b)) and the temperature
126 at the top of the troposphere. Assuming an almost constant temperature in the strato-
127 sphere, a fixed altitude, high enough to be above the tropopause in the whole globe, has
128 been taken. This level has been chosen at 100 hPa, obtained from ERA5 data on pres-
129 sure levels; Hersbach et al. (2018a)). The results do not vary significantly when more com-
130 plex algorithm is used to define the temperature field. Tropospheric temperatures were
131 translated into equivalent depth fields using eq. (3), which in turn were incorporated into
132 the model through the bathymetry. As such, the bathymetry field was updated every
133 hour to take into account air temperature variations estimated from ERA5 hourly data.

134 The initial perturbation created by the volcano eruption was simulated using an
135 equivalent atmospheric pressure perturbation of 50 hPa. In the model, this was intro-
136 duced as an instantaneous sea level perturbation at the start of the simulation, which
137 had a cylinder-like shape of 60 km radius and 50 cm height. The intensity and the ex-
138 tend of the initial perturbation were chosen to match the amplitude and frequency of
139 the available atmospheric pressure records from Fig. 2. Other shapes such as a Gaus-
140 sian and semi-spherical perturbations were also tested for the initial forcing with sim-
141 ilar results.

142 The outputs of the hydrodynamic model are provided as sea surface displacements.
143 We apply the inverted barometer equivalence to convert the sea level response into an
144 atmospheric pressure signal. This approach corresponds to a decrease of 1 hPa for ev-
145 ery cm of water elevation, and vice versa. The simulation took a total of 6 h to complete
146 with 23 CPU.

147 The simulation was validated against in-situ surface atmospheric pressure records
148 obtained from different sources (see the map in Fig. 2 to see the spatial distribution of
149 the stations). A total of 889 station were retrieved from NOAA Automated Surface/Weather
150 Observing Systems (ASOS/AWOS) spread across all United States, including Hawaii,
151 Alaska and Puerto Rico. A time series of atmospheric pressure from Ciutadella (Balearic
152 Islands, Spain) with a temporal resolution of 30 seconds was obtained from the Balearic
153 Islands Coastal Observing and Forecasting System (SOCIB). Another time series from
154 Kadhdhoo, in the Maldives, with a 10 minutes temporal resolution was also used to com-
155 pare with the model outputs. Atmospheric pressure records where also obtained from
156 the Australian Bureau of Meteorology at three locations (Sydney Observatory Hill, Perth

157 Airport and Darwin Airport) with 1 minute temporal resolution. Among all the atmo-
158 spheric pressure records, only those with less than 10% of missing values were retained,
159 which left a total of 719 stations (20% of them were removed). Since the period of the
160 generated Lamb wave was around 40 minutes, the atmospheric pressure records were band-
161 pass filtered with cut-off periods between 2 hours and 15 minutes. In each record, the
162 first pass of the atmospheric perturbation was identified as the first maximum of the time
163 series after the explosion (this peak was required to exceed 3 times the standard devi-
164 ation of the filtered time series). In 42 of these time series no peak was larger than the
165 threshold imposed and were consequently discarded. Additional 56 time series were also
166 discarded because the detected peak clearly corresponded to a different atmospheric pro-
167 cess. The total number of stations used was 621.

168 The simulation was also qualitatively compared to satellite observations to further
169 assess the realism of the wave propagation. Infrared data from the Geostationary Op-
170 erational Environmental Satellite (GOES-R) program and the European Organisation
171 for Exploitation of Meteorological Satellites (EUMETSAT) were used at 15-min tem-
172 poral resolution for the first 24 hours since the eruption. The Pacific region was repre-
173 sented by the GOES-17 satellite with imagery from the IR10.3 channel with a spatial
174 resolution of 5424×5424 pixels. The 0-degree region was observed by the Meteosat-11
175 satellite (High Rate SEVIRI Level 1.5 Image Data) with data from the IR10.8 channel
176 with a spatial resolution of 3712×3712 pixels. For the sake of visualization of the at-
177 mospheric pressure wave footprint in the satellite IR observations we used, at each time
178 step, their second time-derivative. These fields were subsequently spatially filtered with
179 a 50 (100) pixel window for GOES-17 (Meteosat-11) satellite observations with the fil-
180 ter described in Amores et al. (2018).

181 3 Results

182 A qualitative comparison of the model results with satellite observations during the
183 first travel of the Lamb waves (from the origin to the antipodes in Northern Africa) re-
184 veals that the simulation closely follows the spatial pattern of the satellite measurements
185 (Fig. 1). Note that we are comparing the observed and modeled spatial footprints of the
186 waves, but using different variables. The relevant parameter here is thus the location of
187 the wave rather than its amplitude. Panels *a-f* show the propagation of the Lamb wave
188 over the Pacific captured by GOES-17 satellite from 15 minutes after the explosion un-
189 til January 15th 10:30 UTC. The wave is clearly observed in satellite images that also
190 display a close agreement with the observations. Panels *g-j* show the travel of the wave
191 captured by Meteosat-11 satellite from 17:30 to 20:30 UTC. In this case, although still
192 identified, the wave signal is surrounded by noisier data probably due to a larger cloud
193 coverage and/or lower spatial resolution offered by this satellite in comparison with GOES-
194 17. The wave is observed at 17:30 and 18:30 and it is still visible at 19:30 and 20:30, co-
195 inciding again with the pattern of the simulation.

196 Fig. 2 shows the comparison of 10 high-frequency atmospheric pressure records (col-
197 ors help matching dots in the map and time series in the lower panel) at different dis-
198 tances from the volcano (indicated with a red star in the map) between January 15th
199 04:30 UTC until January 18th 02:40 UTC. In addition, the temporal evolution of the sim-
200 ulation is available in Movie S1 in the Supplementary Material. The modeled time se-
201 ries (in grey) were extracted from the closer grid point to each station. At all locations
202 the numerical simulation matches very well the time of arrival of the Lamb wave. At each
203 site, 4 different passes are observed, except in the Ciutadella station (dark red), the clos-
204 est to the volcano's antipodes in our database. In this station only two passes occur be-
205 cause of the overlapping of the northern and southern waves (see Movie S1 for a better
206 visualization). The model better captures the first wave pass, as shown by both the ar-
207 rival time and the wave amplitude. Once the Lamb wave has traveled farther distances

208 and has interfered with its own and the environment, the patterns become more com-
209 plex. However, the model is still able to correctly capture the arrival time in most cases.

210 Using all available atmospheric pressure records, we have quantified the performance
211 of the approach by comparing the time of arrival of the first Lamb wave. To do so, we
212 have determined the time when the first atmospheric pressure maximum is found at in-
213 situ pressure records and in the model simulation. Fig. 3 represents the scatter plot of
214 modeled vs. observed arrival times of the first wave. There is an excellent agreement be-
215 tween model and observations at all sites, with a R^2 larger than 0.98 and a root mean
216 square difference (RMSD) of 10 minutes (we remark here that the temporal resolution
217 of the simulation is 5 minutes).

218 4 Summary and Conclusions

219 After Hunga-Tonga volcano explosion on January 15th, 2022, atmospheric pressure
220 records around the world measured high-frequency perturbations that traveled around
221 the globe several times and that were consistent with the presence of atmospheric Lamb
222 waves. We have numerically simulated the atmospheric Lamb waves generated by the
223 volcanic eruption taking advantage of their similarities to ocean long waves. Namely, both
224 types of waves propagate through the fluid as vertically integrated waves, with 2D hor-
225 izontal motion and share the same dispersion relation. The analogy consists of defining
226 an equivalent bathymetry in the ocean shallow water model that corresponds to the ver-
227 tically averaged air temperature, which has furthermore temporal variability.

228 The results of the simulation mimic satellite and in-situ observations. In partic-
229 ular, when the outputs of the model are compared to atmospheric pressure records at
230 different distances from the source, they display excellent matching in the arrival times
231 of the perturbation. Therefore, the results confirm that the observed high-frequency sur-
232 face pressure oscillations are the footprint of non-dispersive atmospheric Lamb waves orig-
233 inated by the eruption of the Hunga-Tonga volcano.

234 Despite being an idealized simulation, which neglects various factors that may af-
235 fect different characteristics of the wave, the close agreement between the observation
236 and the model suggests that the main physical mechanisms are well represented in our
237 experiment. For example, our model does not consider the effect of orography. High moun-
238 tain systems such as the Andes or Himalayas may cause reflections of the Lamb waves
239 that are not represented in our simulation. We also made some assumptions in our ap-
240 proach, but they do not prevent us from correctly simulating the wave propagation. For
241 example, we assumed the temperature to be constant in the vertical through the tropo-
242 sphere, but we found that using the average temperature was a good approximation to
243 estimate the equivalent depth. We also assumed the air to be dry and thus, we consid-
244 ered that water vapor and humidity changes have only a minor effect on the propaga-
245 tion of the wave. In summary, we have shown how a vertically integrated hydrodynamic
246 ocean model can be used to investigate and anticipate the propagation of atmospheric
247 Lamb waves across an isotherm troposphere.

248 Conflict of Interest

249 The authors declare no conflicts of interest relevant to this study.

250 Open Research

251 Data Availability Statement:

- 252 • ERA5 dataset can be downloaded from <https://cds.climate.copernicus.eu/>.

- 253 • NOAA atmospheric pressure time series were downloaded from <https://mesonet.254 agron.iastate.edu/request/asos/1min.phtml#>).
- 255 • SOCIB data is available in <https://www.socib.es/?seccion=observingFacilities&facility=256 mooring>.
- 257 • Information regarding the Maldivian atmospheric pressure record can be found 258 in <https://mv.geoview.info/kadhdhoo,7909905>.
- 259 • The GOES satellite data can be downloaded from <https://www.ncdc.noaa.gov/260 airs-web/search>.
- 261 • The Meteosat-11 data was obtained from <https://navigator.eumetsat.int/262 product/E0:EUM:DAT:MSG:HRSEVIRI>.

263 The numerical simulation can be downloaded from: <https://doi.org/10.5281/zenodo.5948860>

264 Acknowledgments

265 This study was supported by the MOCCA project RTI2018-093941-B-C31 funded by MCIN/AEI
266 /10.13039/501100011033/ and by FEDER Una manera de hacer Europa. It was also sup-
267 ported by grants PGC2018-099285-B-C21 and PGC2018-099285-B-C22 funded by MCIN/AEI/
268 10.13039/501100011033 and by “ERDF A way of making Europe” NextGenerationEU/PRTR.
269 Angel Amores was funded by the Conselleria d’Educació, Universitat i Recerca del Gov-
270 ern Balear through the Direcció General de Política Universitària i Recerca and by the
271 Fondo Social Europeo for the period 2014–2020 (grant no. PD/011/2019). Daniel Argüeso
272 was funded by Spanish Ministry of Science and Innovation through the EPICC Project
273 (PID2019-105253RJ-I00) and the Beatriz Galindo Programme (BG20/00078). The au-
274 thors are grateful to NOAA, EUMETSAT, the Australian Bureau of Meteorology and
275 SOCIB to make their data freely available. Finally, we also thank to Dr. Ali Shareef for
276 providing the atmospheric pressure data from the Maldives.

277 References

- 278 Adam, D. (2022). Tonga volcano eruption created puzzling ripples in Earth’s atmo-
279 sphere. *Nature*. doi: 10.1038/d41586-022-00127-1.
- 280 Amores, A., Jordà, G., Arsouze, T., & Le Sommer, J. (2018). Up to what extent
281 can we characterize ocean eddies using present-day gridded altimetric prod-
282 ucts? *Journal of Geophysical Research: Oceans*, *123*(10), 7220–7236. doi:
283 <https://doi.org/10.1029/2018JC014140>
- 284 Cronin, S. J., Brenna, M., Smith, I., Barker, S., Tost, M., Ford, M., ... Vaiomounga,
285 R. (2017). New volcanic island unveils explosive past. *EOS*, *98*. doi:
286 <https://doi.org/10.1029/2017EO076589>
- 287 Global Volcanism Program. (2022). Report on Hunga Tonga-Hunga Ha’apai
288 (Tonga). *Bulletin of the Global Volcanism Network, Smithsonian Institution*,
289 *40:1*. doi: <https://doi.org/10.5479/si.GVP.BGVN201501-243040>
- 290 Gossard, E., & Hooke, W. (1975). *Waves in the atmosphere*. Amsterdam: Elsevier.
- 291 Hersbach, H., Bell, B., Berrisford, P., Biavati, G., Horányi, A., Muñoz Sabater, J.,
292 ... Thépaut, J.-N. (2018a). ERA5 hourly data on pressure levels from 1979 to
293 present. *Copernicus Climate Change Service (C3S) Climate Data Store (CDS)*.
294 doi: 10.24381/cds.bd0915c6
- 295 Hersbach, H., Bell, B., Berrisford, P., Biavati, G., Horányi, A., Muñoz Sabater, J.,
296 ... Thépaut, J.-N. (2018b). ERA5 hourly data on single levels from 1979 to
297 present. *Copernicus Climate Change Service (C3S) Climate Data Store (CDS)*.
298 doi: 10.24381/cds.adbb2d47
- 299 Klein, A. (2022). Tongan volcano erupts. *New Scientist*, *253*(3370), 7. Re-
300 trieved from [https://www.sciencedirect.com/science/article/pii/](https://www.sciencedirect.com/science/article/pii/S0262407922000744)
301 [S0262407922000744](https://www.sciencedirect.com/science/article/pii/S0262407922000744) doi: [https://doi.org/10.1016/S0262-4079\(22\)00074-4](https://doi.org/10.1016/S0262-4079(22)00074-4)
- 302 Lamb, H. (1881). On the vibrations of an elastic sphere. *Proceedings of*

- 303 *the London Mathematical Society*, *s1-13*(1), 189-212. Retrieved from
304 [https://londmathsoc.onlinelibrary.wiley.com/doi/abs/10.1112/plms/](https://londmathsoc.onlinelibrary.wiley.com/doi/abs/10.1112/plms/s1-13.1.189)
305 [s1-13.1.189](https://londmathsoc.onlinelibrary.wiley.com/doi/abs/10.1112/plms/s1-13.1.189) doi: <https://doi.org/10.1112/plms/s1-13.1.189>
- 306 Monserrat, S., Vilibić, I., & Rabinovich, A. B. (2006). Meteotsunamis: atmo-
307 spherically induced destructive ocean waves in the tsunami frequency band.
308 *Natural Hazards and Earth System Sciences*, *6*(6), 1035–1051. Retrieved
309 from <https://nhess.copernicus.org/articles/6/1035/2006/> doi:
310 [10.5194/nhess-6-1035-2006](https://doi.org/10.5194/nhess-6-1035-2006)
- 311 Murty, T. S. (1977). Seismic sea waves: tsunamis.
- 312 Press, F., & Harkrider, D. (1966). Air-Sea Waves from the Explosion of Kraka-
313 toa. *Science*, *154*(3754), 1325-1327. Retrieved from [https://www.science](https://www.science.org/doi/abs/10.1126/science.154.3754.1325)
314 [.org/doi/abs/10.1126/science.154.3754.1325](https://www.science.org/doi/abs/10.1126/science.154.3754.1325) doi: [10.1126/science.154](https://doi.org/10.1126/science.154)
315 [.3754.1325](https://doi.org/10.1126/science.154.3754.1325)
- 316 Symons, G. J. (ed.). (1888). The eruption of Krakatoa and subsequent phenomena.
317 *Report of the Krakatoa Committee of the Royal Society*.
- 318 Titov, V., Rabinovich, A. B., Mofjeld, H. O., Thomson, R. E., & González, F. I.
319 (2005). The global reach of the 26 december 2004 Sumatra tsunami. *Science*,
320 *309*(5743), 2045-2048. doi: [10.1126/science.1114576](https://doi.org/10.1126/science.1114576)
- 321 Zhang, Y., & Baptista, A. M. (2008). SELFE: A semi-implicit Eulerian–Lagrangian
322 finite-element model for cross-scale ocean circulation. *Ocean Modelling*, *21*(3),
323 71-96. doi: <https://doi.org/10.1016/j.ocemod.2007.11.005>
- 324 Zhang, Y. J., Ye, F., Stanev, E. V., & Grashorn, S. (2016). Seamless cross-scale
325 modeling with SCHISM. *Ocean Modelling*, *102*, 64-81. doi: [https://doi.org/10](https://doi.org/10.1016/j.ocemod.2016.05.002)
326 [.1016/j.ocemod.2016.05.002](https://doi.org/10.1016/j.ocemod.2016.05.002)

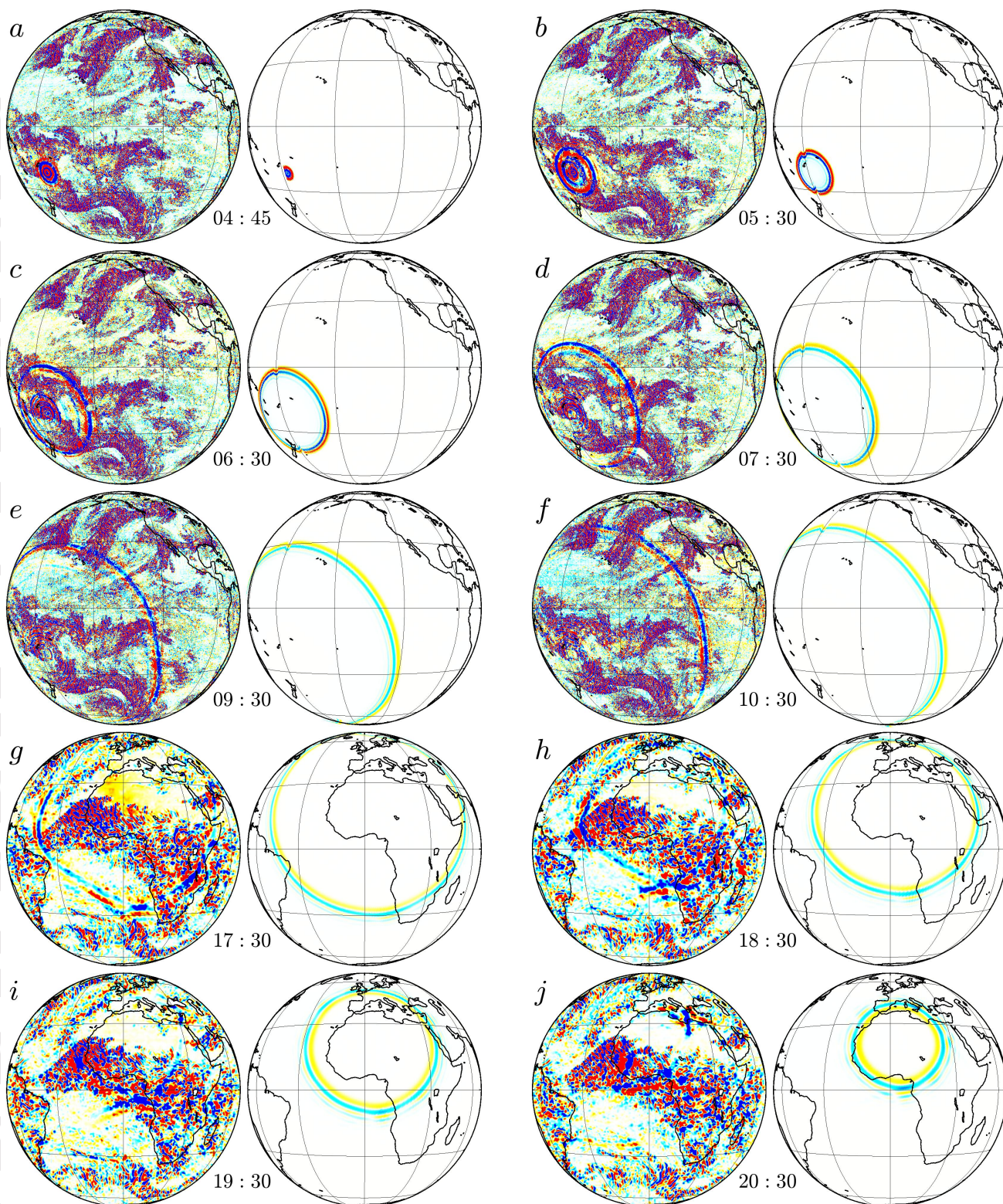


Figure 1. Comparison of the Lamb wave observed from satellite observations and the numerical simulation during January 15th, 2020 at different times. Each panel shows the satellite observations at left and the corresponding simulation field at the right. Panels *a* to *f* correspond to observations from GOES-17 satellite while panels *g* to *j* correspond to observations from Meteosat-11 (see in the Data and Methods sections the details of the postprocessing performed). The colorscales are different for each satellite and numerical simulation and are fixed to provide a correct visualization.

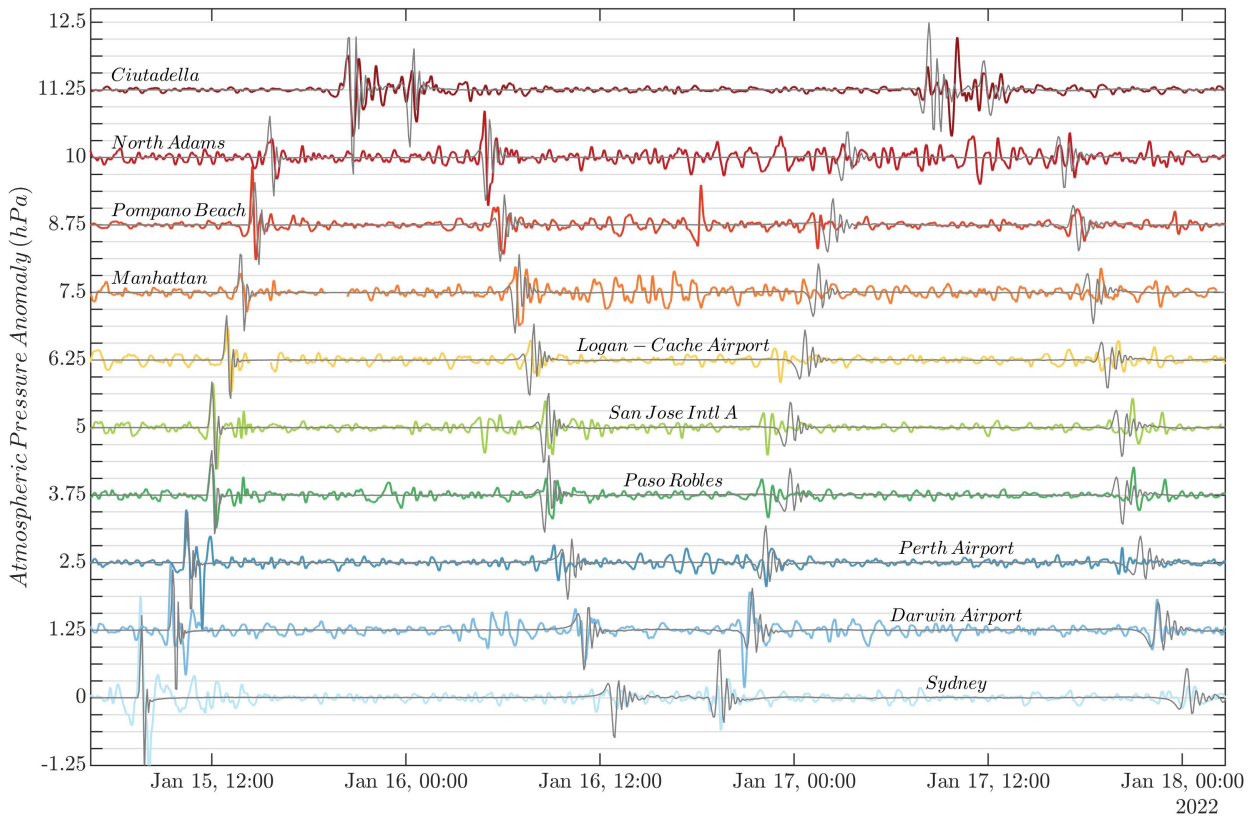
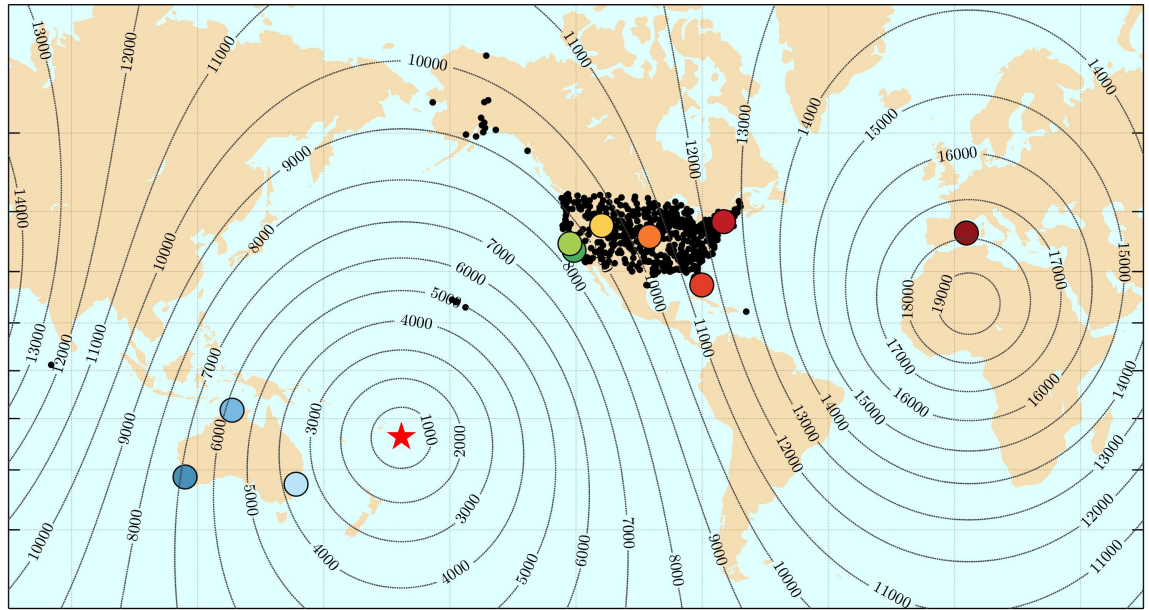


Figure 2. The upper panel shows the location from where all atmospheric pressure records used were measured (black and colored dots). The red star indicated the location of the explosion. Contour lines indicate the distance from the location of the explosion in km. The lower panel shows the comparison between 10 atmospheric pressure anomaly records (in different colors corresponding to the colored points from the upper panel) and the numerical simulation record at the closest grid point (black lines) from January 15th 04:30 UTC until January 18th 02:40 UTC. The different stations shown were selected to cover different distances from the origin of the Lamb wave.

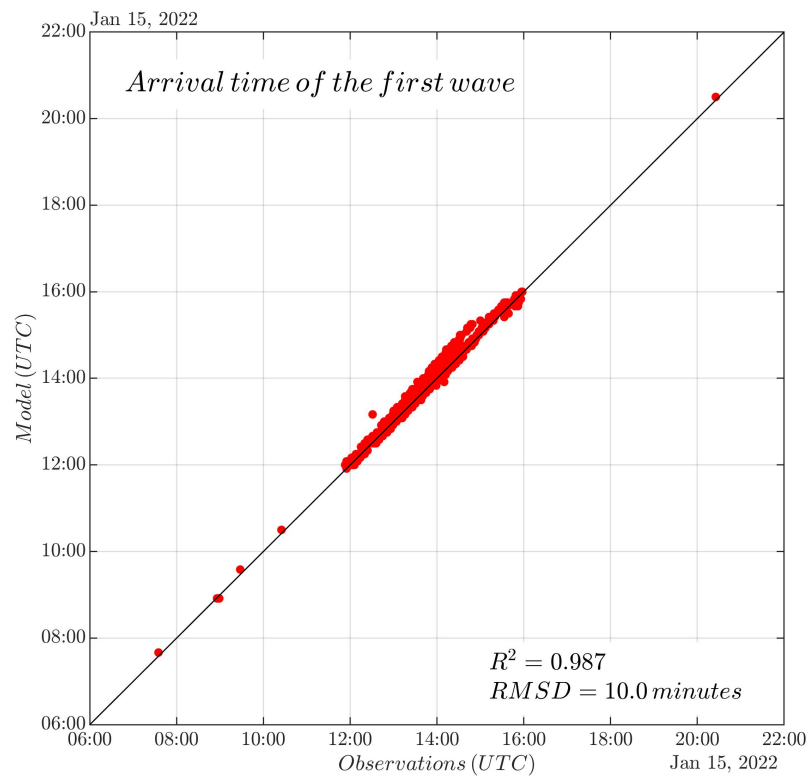


Figure 3. Comparison between the modeled arrival time of the first pass of the Lamb wave as a function of the observed arrival time.